Progress in Propulsion Physics **11** (2019) 25-64
https://doi.org/10.1051/eucass/201911025

THE HyEnD STERN HYBRID SOUNDING ROCKET PROJECT

M. Kobald[1], C. Schmierer[1,2], U. Fischer[1,2], K. Tomilin[1,2], A. Petrarolo[1], and M. Rehberger[1]

[1]DLR, Institute of Space Propulsion
Langer Grund, Hardthausen 74239, Germany

[2]Institute of Space Systems, University of Stuttgart
29 Pfaffenwaldring, Stuttgart 70569, Germany

The student team Hybrid Engine Development (HyEnD) of the University of Stuttgart is taking part with the Institute of Space Systems (IRS) in the DLR educational program STERN (Studentische Experimentalraketen). This program supports students at German universities to design, build, and launch an experimental rocket within a 3-year project time frame. HyEnD is developing a hybrid rocket called HEROS (Hybrid Experimental Rocket Stuttgart) with a design thrust of 10 kN, a total impulse of over 100 kN·s, and an expected liftoff weight up to 175 kg. HEROS is planned to be launched in October 2015 from Esrange in Sweden to an expected flight altitude of 40 to 50 km. The current altitude record for amateur rockets in Europe is at approximately 21 km. The propulsion system of HEROS is called HyRES (Hybrid Rocket Engine Stuttgart) and uses a paraffin-based solid fuel and nitrous oxide (N_2O) as a liquid oxidizer. The development and the test campaign of HyRES is described in detail. The main goals of the test campaign are to achieve a combustion efficiency higher than 90% and provide stable operation with low combustion chamber pressure fluctuations. The successful design and testing of the HyRES engine was enabled by the evaluation and characterization of a small-scale demonstrator engine. The 500-newton hybrid rocket engine, called MIRAS (MIcro RAkete Stuttgart), has also been developed in the course of the STERN project as a technology demonstrator. During this test campaign, a ballistic characterization of paraffin-based hybrid rocket fuels with different additives in combination with N_2O and a performance evaluation were carried out. A wide range of operating conditions, fuel compositions, injector geometries, and engine configurations were evaluated with this engine. Effects of different injector geometries and postcombustion chamber designs on the engine

performance were analyzed. Additionally, the appearance of combustion instabilities under certain conditions, their effects, and possible mitigation techniques were also investigated. Concluding, the development and construction of an advanced, lightweight hybrid sounding rocket for the given requirements and budget within the DLR STERN program are described herein. The most important parts include a high thrust hybrid rocket engine, the development of a light weight oxidizer tank, pyrotechnical valves, carbon fiber rocket structure, recovery systems, and onboard electronics.

ABBREVIATIONS

CFRP	Carbon-fibre reinforced plastic
DLR	Deutsches Zentrum für Luft- und Raumfahrt (German Aerospace Center)
FEP	Fluorinated ethylene propylene
FFT	Fast Fourier transform
GOx	Gaseous oxygen
HDPE	High-density polyethylene
HEROS	Hybrid Experimental Rocket Stuttgart
HTPB	Hydroxyl-terminated polybutadien
HyEnD	Hybrid Engine Development, DGLR student group
HyRES	Hybrid Rocket Engine Stuttgart
LOx	Liquid oxygen
MIRAS	Micro Rakete Stuttgart (demonstrator rocket)
MORABA	Mobile Raketenbasis (DLR sounding rocket division)
N_2O	Nitrous oxide
PTFE	Polytetrafluoroethylene
RES	Recovery & Electronics Section
S/A	Safety and arming device
SA	Stearic acid
STERN	STudentische Experimental RaketeN (Student Experimental Rockets, educational program of DLR)

NOMENCLATURE

a, n, m	Ballistic coefficients
A_{eff}	Effective drag area
A_t	Nozzle throat area
c	Average speed of sound in the chamber
c^*	Characteristic velocity
C_D	Drag coefficient of the parachute

D_t	Nozzle throat diameter
F	Thrust
F_{op}	Dynamic opening load
G	Propellants mass flux
G_{Ox}	Oxidizer mass flux
I_{sp}	Specific impulse
l	Nozzle length
L	Total combustion chamber length
L_{fuel}	Fuel grain length
$\dot{m}_{\text{Ox}}$	Oxidizer mass flow
OF	Oxidizer to fuel mixture ratio
P_c	Chamber pressure
$\dot{r}$	Regression rate
Sr	Strouhal number
t_b	Burning time
V	Combustion port total volume
V_L	Landing speed
V_{op}	Descendent rate
ρ	Air density

1 INTRODUCTION TO HyEnD

Hybrid Engine Development is a student based project located at the University of Stuttgart, since its foundation in 2006. From 2006 to 2012, HyEnD focused on developing its own hybrid rocket engines in different scales from 250- to 2000-newton thrust [1]. In 2012, the project Studentische Experimentalraketen (student experimental rockets, STERN, [2]) was initiated by the German Aerospace Center (DLR) and HyEnD applied for it with the Institute of Space Systems. The gained experience and knowledge of HyEnD in developing and testing hybrid rocket engines was the foundation to develop, construct, and build its own experimental hybrid sounding rocket within three years of the STERN project.

In September 2012, the rocket development began, starting from scratch. Except for the rocket engine, HyEnD had only little experience with the rocket systems including flight-weight propellant management, rocket recovery, and flight electronics. Within the first year, the concept of the rocket called HEROS was developed. Simultaneously, a smaller demonstrator rocket called MIRAS was initiated in order to test all subsystems in a smaller scale before the launch of HEROS in 2015. HEROS was targeted to have a thrust of 10 kN and an altitude of more than 20 km. A smaller scale was applied for MIRAS, which reaches altitudes of around 2 km with a 500-newton engine. This allows to test the rocket on German launch sites. Both MIRAS and HEROS use a hybrid rocket engine with a paraffin-based fuel and liquid N_2O as oxidizer. More than 140 hot-fire tests

Table 1 HyEnD-STERN project time line at University of Stuttgart (July 2015)

Date	Task
2006	Foundation of HyEnD
2008	First hybrid rocket engine test campaign
September 2012	Begin of STERN project at HyEnD
September 2013	Begin of MIRAS 500-newton engine test campaign
December 2013	**Preliminary Design Review**
November 2014	Begin of HyRES 10-kilonewton engine test campaign
November 2014	**Critical Design Review**
February 2015	1st launch of MIRAS
May 2015	**Integration Progress Review**
July 2015	*End HyRES test campaign*
August 2015	*2^{nd} MIRAS launch*
August 2015	*Completion of HEROS integration*
September 2015	***Rocket Acceptance Review***
October 2015	***Flight Readiness Review***
October 2015	*HEROS launch*
November 2015	*Postflight analysis*

have been performed in the HyEnD project so far. Results of the 500-newton engine development are presented in [3], the design of the HEROS hybrid sounding rocket is presented in detail in [4]. During the development of the MIRAS demonstrator, a lot of improvements were made to the design of different subsystems which were applied to the HEROS rocket design until the end of the 2nd year. At that time, HyEnD also passed the Critical Design Review. The review board included experts from the DLR MORABA, the DLR Space Agency, and the DLR Institute of Space Propulsion. In early 2015, the MIRAS demonstrator rocket was launched successfully, proving that the baseline concept is working. In summer 2015, a 2nd flight of MIRAS is planned before the launch campaign of HEROS in October 2015. It is planned to take place at the Esrange Space Center near Kiruna, Sweden. The latest project advancement was the successful Integration Progress Review in May 2015. A time line is given in Table 1, italic text was used for future events.

2 STATE-OF-THE-ART OF HYBRID ROCKET PROPULSION

Hybrid rocket engines are in the focus of research at several institutions and universities world wide. They are well suited for educational purposes with students due to their inherent safety. Especially small-scale combustion experiments are

widely available and described in detail in the literature. At larger scale, the number of experiments and available data is much smaller. Their good performance, depending on the chosen propellant combination, makes hybrid rockets attractive for small to medium scale sounding rockets. The throttling and restart capability are further advantages of hybrid rocket engines.

At large scale, the biggest operational hybrid rocket engine was realized within the Hybrid Propulsion Demonstration Program in the United States [5]. The engine was based on hydroxyl-terminated polybutadien (HTPB) and liquid oxygen (LOx) with a thrust of 250 klb. Subscale tests were successful while the full thrust engine still suffered from instabilities [6]. Recent efforts from NASA Ames, the Stanford University, and the Space Propulsion Group were aiming at developing the Peregrine sounding rocket in a joint program. It uses a hybrid rocket engine with N_2O and a paraffin-based fuel to launch a 5-kilogram payload to an altitude of more than 100 km [7–12]. The development of the engine was challenging due to the occurrence of low-frequency instabilities based on feed system coupling and acoustic instabilities [11, 12]. The low-frequency instabilities were partially related to the injection conditions of the N_2O, especially its vapor pressure [13–15]. The latest tests showed stable operation at high efficiency. In the last years, the Space Propulsion Group developed a high performance hybrid rocket engine with LOx and paraffin-based fuels as propellants [16, 17]. Its application was proposed as an upper stage engine where it should have an extrapolated vacuum specific impulse of 340 s. The technological challenges of combustion instabilities that often arise with LOx hybrid rocket engines [18] were said to be solved only by advanced combustion chamber and injector design and passive devices. In previous engines, these instabilities were only solved partially by injecting pyrophoric liquids, which increased the complexity and decreased the inherent safety of hybrid rocket engines [19–21]. The JAXA in Japan is investigating a wide field of different hybrid rocket propulsion concepts [22]. A scale-up engine was set up with gaseous oxygen (GOx) or LOx at 5-kilonewton thrust and swirl injection. At Padua, a hybrid rocket booster was developed with total impulse of 50 kN·s and a short burn time [23]. Space Ship One and Two are still the most well known examples of flight proven hybrid rocket engines. Recently, the research at German universities in small sounding rockets with hybrid rocket engines has increased thanks to the aforementioned DLR STERN program. It was initiated by the DLR Space Administration to promote the interest of students and young professionals for launcher systems and space transportation [2].

Concluding, it is seen that combustion instability is a design challenge for these types of engines at increased scale and a special focus is set on this point during the development program. In general, combustion instability was and still is a key element for all types of rocket engines: liquids, solids, and hybrids.

3 HEROS ROCKET SYSTEM OVERVIEW

HEROS consists of the following subsystems which are shown in Fig. 1:

- hybrid rocket engine HyRES;
- remote controlled oxidizer loading system:
  - quick connect to oxidizer loading arm;
  - check valve;
  - pyrotechnical release valve;
  - safety valve;
- recovery system:
  - pilot parachute;
  - break parachutes;
  - main parachute;
  - release mechanisms;
- oxidizer tank;
- pyrotechnical valve;
- onboard electronics:
  - measurement system; and
  - telemetry and recovery deployment; and

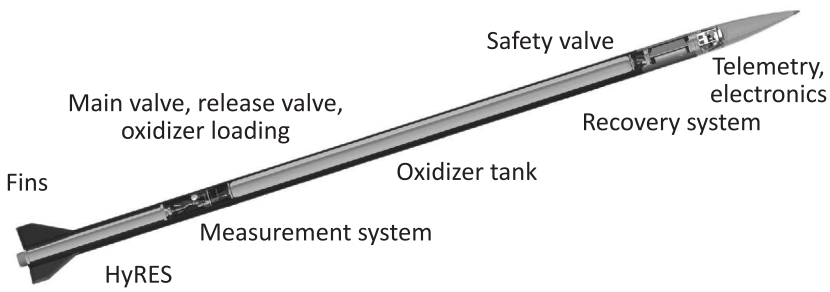

Figure 1 Overview of HEROS rocket and its subsystems

– rocket structure:
  - hull;
  - connectors;
  - nose-cone; and
  - fins.

In addition to the systems which make up the actual rocket, a lot of work and effort has been invested in the global small engines. It will be used at Esrange to load or unload the oxidizer, supply the rocket with power while on launch pad, operate the onboard electronics and cameras, and provide a remote connection to the control room at the Esrange launch site.

3.1 Propulsion System

3.1.1 HyRES hybrid rocket engine

An efficient and stable rocket engine is mandatory for a sounding rocket that shall reach high altitudes. A hybrid rocket engine was chosen for the HyEnD project due to its good performance and inherent safety. That makes it especially useful to work within educational programs with students. The oxidizer is N_2O and a solid paraffin-based fuel are used. The usage of liquefying fuels enables a simple single port fuel designs and a higher fuel utilization compared to low regression rate fuels like HTPB. The application of a self-pressurizing oxidizer permits a simple propulsion system with good performance, without external pressurization. The surface of the paraffin fuel forms a liquid melt layer during the combustion due to the low melting point of paraffin. This liquid layer creates droplets from hydrodynamical unstable waves, which are increasing the regression rate of the fuel by a factor of 3 to 6, compared to classic hybrid rocket fuels like HTPB [24]. Detailed research regarding this kind of fuel was done in cooperation with the DLR Institute of Space Propulsion, Lampoldshausen [25]. The fuel of HyRES was designed for a high performance in regression rate and mechanical properties. Furthermore, a lot of effort was put in the increase of the combustion efficiency. It is low for hybrid rocket engines, if the combustion chamber design is not optimized. The reason for this is that a complete mixing

Table 2 HyRES key data

Property	Value
Nominal thrust	10 kN
Nominal burn time	18 s
Nominal mass flow	5–5.5 kg/s
Chamber pressure	30–35 bar
Solid paraffin-based fuel	12.5 kg
Combustion efficiency	$> 95\%$
Dry mass	21 kg
Length	1300 mm
Fuel diameter	175 mm

of the fuel and the oxidizer does not happen directly after injection, but the fuel mass flow is distributed over the length of the chamber. This forms, typically, a layered flow structure where the fuel is outside while the oxidizer is in the core. To optimize this, different injectors, mixture ratios, and combustion chamber layouts were investigated. Table 2 shows the key operational data of HyRES.

3.1.2 Oxidizer tank

The largest single component of the rocket is the oxidizer tank. It has a volume of more than 100 l and a length of about 4 m. It will contain over 80 kg of N_2O in liquid state at about 55 bar. HEROS uses the ability of self-pressurization of the N_2O. This means there is no pump or secondary pressurization with a gas. The vapor pressure of N_2O is about 55 bar at an ambient temperature of 25 °C. When the tank empties during the burn of the engine, the pressure drops but additional N_2O evaporates. This lowers the tank pressure nearly at a constant rate for the nominal burn duration. At the end of the burn time, only gaseous N_2O is left in the tank, which will flow out into the chamber and provide additional thrust, although it is very low compared to the nominal thrust. This kind of self-pressurization allows to spare a pressurization system or a pump but in return, additional oxidizer has to be loaded which is mainly used to pressurize the tank and only creates a small amount of thrust and impulse during combustion. Since N_2O is also near the critical point at the storing conditions in the tank, the density of the gaseous phase is quite high. Therefore, the complete tank filling of gaseous N_2O is about 25 kg at the end of the burn. Due to this setup, the tank needs to have an operating pressure of 60 bar. According to the safety requirements of Esrange, where the rocket is planned to be launched, a safety factor of at least 2 has to be applied to all pressurized systems. From these requirements, it was concluded at the beginning of the design of the rocket that the oxidizer tank needs to be optimized regarding light-weight construction. Initially, a simple aluminum tank was analyzed. It was a feasible option but in order to reduce the dry mass, a tank of smaller size would have been chosen, resulting in a shorter burning time of the engine. Even then, the dry mass of a smaller aluminum tank would have been 35 to 40 kg. So, the next step was taken to design a carbon-fibre reinforced plastic (CFRP) tank in a student thesis [26]. There were problems identified with the compatibility of N_2O and the organic components of CFRP resins. It is not proven that CFRP and N_2O are compatible and there are results indicating that parts of the organic resin dissolve over time into the N_2O. This lowers the temperature of self-ignition drastically and, thereby, the safety [27]. This is also a problem with some commercially available liner materials for CFRP tanks which are mostly polymers. One group of polymers that has been proven to be compatible with N_2O over a wide range of applications are fluoropolymers like polytetrafluoroethylene (PTFE) or fluorinated ethylene

Figure 2 Oxidizer tank aluminum liner after welding, photo by KWM Weißhaar GmbH

propylene (FEP). Therefore, it was investigated to build a fluoropolymer liner and wrap it in CFRP. Due to manufacturing problems and difficulties to find industrial suppliers for a fluoropolymer liner in this size, the design was put on a hold for possible later uses to stay within the schedule of the STERN program. Smaller demonstrator tanks have been produced with a FEP liner where it was proven that the concept works. If a manufacturing process for a very thin FEP or PTFE liner will be established in the future, the weight of the oxidizer tank would be reduced down to less than 15 kg for a tank volume of 100 l of N_2O.

Instead, a compromise regarding the system weight was found by using a welded aluminum liner and reinforce it with CFRP. By doing this, the total mass of the oxidizer tank was reduced compared to the pure aluminum design to about 25 kg and at the same time, the volume was increased up to more than 100 l. The welded aluminum liner was produced out of 4 parts: 2 tubes of 1.85-meter length and 2 end caps with integrated threads for Swagelok adapters. The tubes of 1.5-millimeter thick aluminum were bended from sheet metal and welded with a longitudinal welding seam. Future tanks could be produced using thinner sheet metal to save more weight but manufacturing processes would get more expensive and for a single tank for an experimental rocket, it might not be cost effective. Figure 2 shows the welded aluminum liner before wrapping with CFRP.

The outer CFRP-laminate of the oxidizer tank is also the outer casing of the rocket and is bearing all mechanical loads during acceleration and recovery phases. This multifunctional design helps to reduce the rocket's structural mass even further. Yet, the defining load for the CFRP coating is the load, which is caused by the pressure of the N_2O inside the tank. For the calculation of the CFRP thickness and fiber orientation, a safety factor of 2 was applied so that the design burst pressure of the composite tank is greater than 120 bar. The tangential force due to pressure is the highest. To compensate all loads, the carbon fibers will be winded in different angles and layers both in tangential and axial directions around the aluminum liner. Classic laminate theory has been used to calculate the stress applied on the CFRP structure. Due to the two-dimensional load onto the tank's structure, a failure model for fiber reinforced

Table 3 The CFRP layer data

Layer	Angle	Thickness, mm
1	20°	0.4
2	−20°	0.4
3	70°	0.8
4	−70°	0.8
5	90°	0.2

plastic is needed to predict the capability of the laminate to withstand the coupled strains. In this case, the ZTL-hypothesis (Zukunftstechnik-Luftfahrt) was used. Table 3 shows the foreseen angles and layer thicknesses. The overall thickness of the CFRP coating will be 2.6 mm. Figure 3 shows the surface structure on the tank after the aluminum liner was winded with CFRP. Since the manufacturing process is also new to our supplying companies, optimizations had to be done during different production steps. In Fig. 4, the finished tank after the winding process is seen.

Figure 3 Complete winding of the aluminum liner in CFRP, photo by CGB (Carbon Großbauteile GmbH)

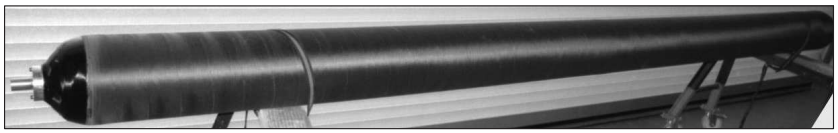

Figure 4 Finished oxidizer tank, photo by CGB

3.1.3 Pyrotechnical valve

Only a few small-scale rockets like HEROS use a liquid propellant. Therefore, there is no commercial off-the-shelf valve suitable for this size. HEROS needs a high mass flow of oxidizer which is around 5 kg/s at about 55 bar. If an off-the-shelf valve suitable for this mass flow was used for the rocket, the mass of this valve would be too high. This was the reason for HyEnD to use a custom

designed valve. Research in historic drawings of valves of the 2nd World War revealed that the pyrotechnical valve of the German "Wasserfall" rocket was a very good valve design, which was used as an inspiration for the valves in the demonstrator rocket MIRAS. Due to its good scalability, it is also used for HEROS. The design of HyEnD's pyrotechnical valve includes a burst disc which is withstanding the pressure of N_2O with a safety factor of more than 2. In other setups, the propellant is often pressurized for opening the burst disc. But this requires a higher operating pressure in the tank which results in a greater dry mass due to thicker walls. Instead, a pyrotechnical charge is ignited to open the main valve for the start of the engine. The opening time is below 0.1 s. Another benefit of the valves design is that no hot gas gets in direct contact with the N_2O. Because N_2O is also a monopropellant, it decomposes exothermically if it is heated to more than 600 °C. Thereby, the valve de-

Table 4 Main valve key data

Parameter	Value
Liquid nominal pressure	60 bar
Safety factor	2.0
Opening time	< 0.1 s
Flow cross-section diameter	25 mm
Pyrotechnical charge mass	< 0.5 g
Total dry mass	< 0.8 kg

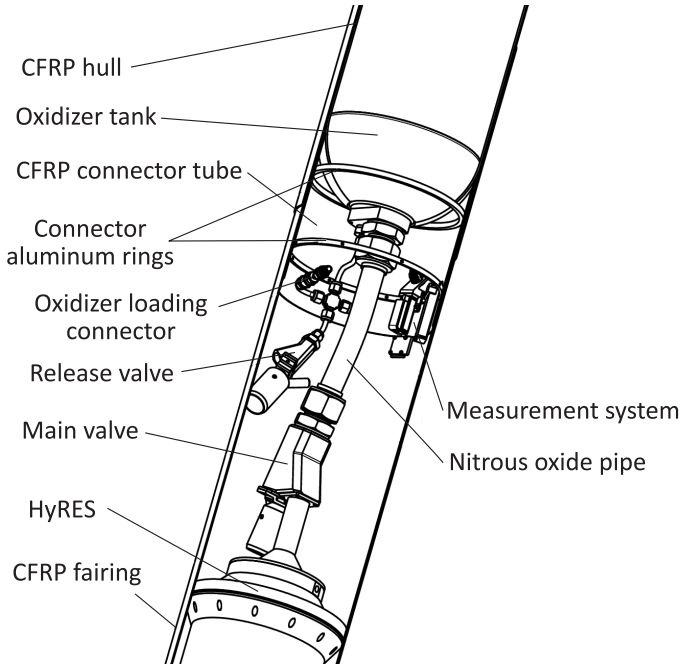

Figure 5 Propulsion system assembly

sign also allows a higher safety with N_2O. Two pyrotechnical valves are used in HEROS. The main valve is used to open the mass flow into the combustion chamber for ignition. The 2nd smaller valve is used if there is a countdown abort and the oxidizer has to be unloaded. The smaller version of the valve, which was used on the demonstrator rocket MIRAS, worked well during tests and the MIRAS maiden flight. Table 4 summarizes the characteristics of HEROS' pyrotechnical valve.

3.1.4 Propulsion system assembly

Table 5 The HEROS propulsion system overview

Parameter	Value
Nominal thrust	10 kN
Nominal burn time	18 s
Dry mass engine	21 kg
Dry mass tank	23 kg
Dry mass valves and tubes	2.5 kg
Total dry mass	46.5 kg
Oxidizer mass	90 kg
Fuel mass	12.5 kg
Total wet mass	149 kg

Figure 5 shows the planned assembly of the propulsion system inside HEROS. The oxidizer tank is on top and the main valve is connecting the HyRES engine and the tank. A flexible hose will connect the tank with the valve. The loading valves and connectors as well as the release valve are connected to the second port of the oxidizer tank. The safety valve is positioned on top of the oxidizer tank. Table 5 shows an overview of the propulsion system of HEROS. The propulsion system makes up roughly 70% of the rocket's dry mass and it takes up the bottom part of the rocket with a length of 6 m.

3.2 Rocket System

3.1.1 Recovery and electronics

A two-stage recovery system was designed to decelerate the entire vehicle to a suitable landing speed. The system comprises two types of parachutes with increasing drag area deploying one after another and enables a wide recovery envelope. A brake cluster of two semielliptical drogue parachutes opens first at the apogee to decelerate the rocket vehicle to a lower air speed at which the toroidal main parachute is safely opened. Due to the high descent rate in the drogue phase, the influence of jet streams and the wind drift is minimized so that a close proximity recovery is performed. Figure 6 shows the design of the complete recovery sequence of HEROS. The Recovery & Electronics Section (RES) has been designed in the course of a student thesis [28].

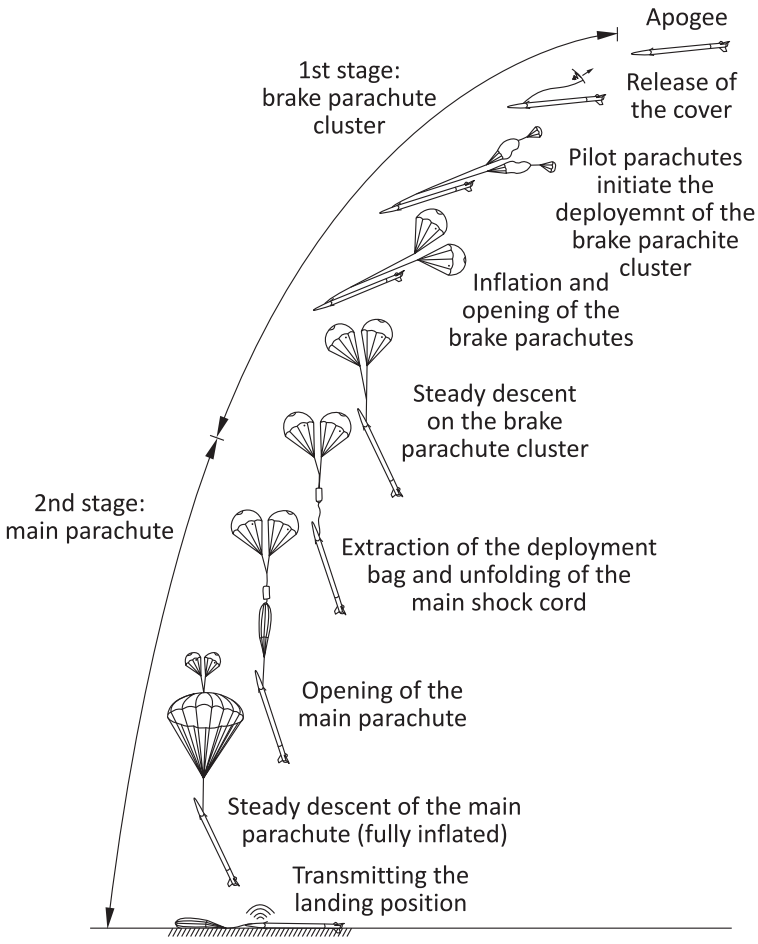

Figure 6 Recovery sequence

Parachute System. The parachutes are stored inside the recovery module, which is located in the bottom part of the RES. At the apogee, the mechanical interlock of the recovery module cover is released, triggered by the flight computer. The cover is pushed away by a compression spring and separates from the recovery section. A pilot parachute is pulled out by the inertia and aerodynamic drag of the cover and initiates the deployment of the brake cluster. The cluster consists of two 0.9-meter semiellipsoid parachutes with an effective drag area of 0.63 m^2 and a drag coefficient $C_D = 1.5$. A vent hole in the canopy apex with the size of 4% of the effective area increases the permeability and provides

high static and dynamic flight stability at the wide range of possible descent rates. As the drag coefficient refers to the homogeneous air flow perpendicular to the entering canopy surface, the C_D of the parachutes within the cluster has to be assumed 25% lower due to the air flow depending on the flight attitude of the cluster. The main parachute deployment occurs, controlled by the flight computer. The toroidal main parachute with an open diameter of 4.3 m and an effective drag area of 13.73 m^2 is stored inside the deployment bag which is pulled out by the aerodynamic drag force of the brake cluster and enables the successive unfolding of the main parachute shock cord and suspensions lines. In addition to the 16 suspension lines, a central line is connected to the vent skirt of the main parachute and leads to the toroidal canopy shape with the drag coefficient $C_D = 2.2$ as given by the manufacturer. The central line and the vent hole reduce the opening shock and prevent sideways oscillations during the descent. In the nominal case, the entire rocket vehicle lands at a speed of 6 m/s. In the case that one of the brake parachutes fails, no flight safety concerns are expected as the main parachute system is able to provide a safe deployment and dissipate all occurring loads up to the descent speed of 40 m/s in the dense atmosphere. In the case of a main parachute system failure, the landing on the brake cluster is possible at a vertical touchdown speed of 25 m/s which significantly minimizes the damage to the vehicle and onboard hardware. The coordinates of the landing site will be transmitted via satellite and Internet by the SPOT Gen3 device, which is integrated inside the RES. Additionally, the positioning data are transmitted by the telemetry unit as a backup. The rocket can be easily dissembled at the landing site after loosening 16 external screws of the tube connector above the oxidizer tank. Afterwards, the rocket will be transported in two pieces of about 6 and 1.5 m in length.

Parameters of the Recovery System Components. Wind tunnel tests on full-scale models have shown that under real conditions, the C_D values given by the manufacturer must be reduced by 10%–15% of the aerodynamic wake of the rocket body. For the average air density ρ at the landing site, the landing speed V_L is calculated with

$$V_L = \sqrt{\frac{2m_{\mathrm{dry}}g}{A_{\mathrm{eff}}\rho C_D}}\,.$$

The descent rate V_{op} at the moment of the main parachute opening is directly proportional to the dynamic opening load F_{op} (opening shock), which is the utmost structural load in the descend phase occurring at the moment of full canopy filling:

$$F_{\mathrm{op}} = 2F_W = \rho V_{\mathrm{op}}^2 C_D A_{\mathrm{eff}}\,.$$

The factor 2 has been verified during wind tunnel tests on full-scale parachute models. The distribution of the aerodynamic drag path from the deployment alti-

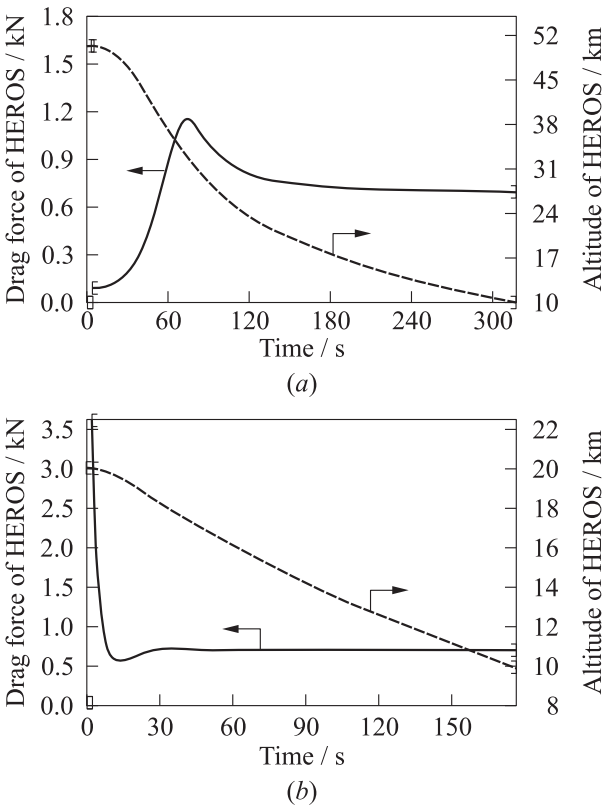

Figure 7 Aerodynamic drag path of the brake cluster deployed at 50 (a) and 20 km (b)

tude of 50 and 20 km is shown in Fig. 7. It was simulated with the Aerospace Trajectory Optimization Software (ASTOS) for a velocity at deployment of 300 m/s and confirms the assumption that the opening shock F_{op} is a correct design parameter for the load-bearing capacity of the parachute system components. The formulas have been evolved according to Lobanov [29] and are reported in detail in [4].

Neither fatigue nor loss of strength of the materials due to the environmental exposures are expected to occur during the operational time. For this reason, a safety factor of $j = 2$ is sufficient.

Deployment System. The deployment system performs a sideways ejection of the parachutes, triggered by the flight computer. It is controlled by the internal altimeter and accelerometer. At the apogee, a pair of pyrotechnical electrical ca-

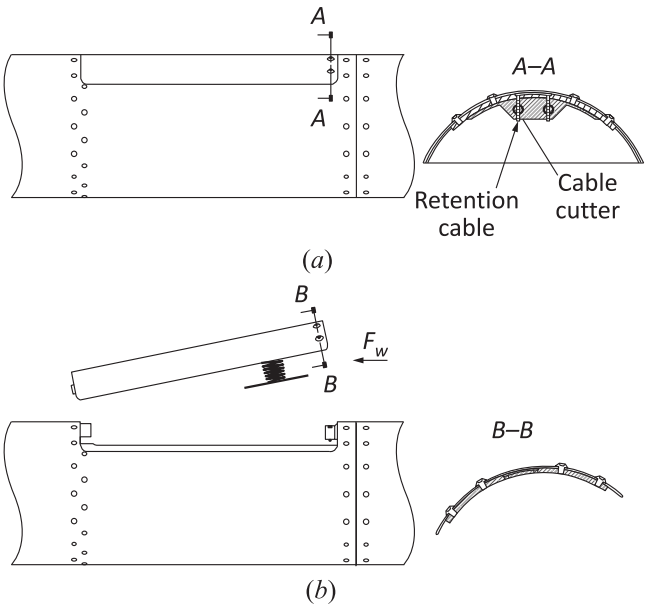

Figure 8 Mechanism of the recovery module cover ejection

ble cutters (CYPRES 2) releases the mechanical interlock of the recovery module cover, which is pushed away by conical compression springs shown in Fig. 8. The separation of the CFRP cover results in the deployment of the brake parachute cluster. The later deployment of the main parachute is initiated by the flight computer after the rocket descends below 1000 m. The second pair of cable cutters releases the loop line of the retaining cord, which is the extension of the brake parachutes shock cord. The retaining cord, made of 4-millimeter Dyneema, enables the force transmission between the brake cluster and the rocket structure during the drogue phase. The system maintenance after landing comprises the renewal of the four cable cutters and of the retention cord. After that and a thorough inspection, the parachute and deployment systems can be used again. The ground and flight safety of the deployment system is ensured by a number of design measures and safety procedures including:

- fail-safe redundant hardware;
- electromechanical safety and arming device (S/A);
- flexible countdown procedure easily adjustable on the launch site's safety constraints; and
- flight path adapted activation logic implemented in the flight computers.

During the launch preparation, the flight computers are turned off for safety reasons. When they are switched on for test purposes, S/A-connectors are set. Thereby, the cutters cannot be initiated which prevents unintended cover ejection. Nevertheless, a removable belt secures the module cover additionally while personnel are near the rocket. Before all persons leave the launching area, the S/A-connector must be disconnected and the securing belt must be removed. The system can stay in this condition for an unlimited time until any remote controlled actions like oxidizer loading on the rocket will be finished. The surveillance of the cover and the retention cords ensures the operational mode of the system. Only as the flight computers are powered on, the operational mode of the cable cutters will change into "ARMED" as the electrical connection to the pyrobatteries is established. The system can stay in this condition for several hours depending on the charge of the batteries. The operational monitoring of the cutters is implemented in the flight computer software. The board continuously sends a low-current pulse which is not sufficient to ignite the cutters. In case of a launch abort, the flight computers must be switched off first, which will disarm the pyrocutters. Personnel should be permitted to approach the launch site only after S/A-connectors have been set by an authorized crew member, which will secure the cutters. After a successful launch and landing, the S/A-connectors must be set manually by an authorized person before further operations on the rocket take place.

Safety and Arming Device. The S/A-connectors provide an electrical shortcut between each cutter and the power supply from the onboard computer. Figure 9 illustrates the safe-mode when the cutters I1 and I2 are not operational due to the connector setting J1 and J2. For the S/A-connectors standard, Lemo plugs and connectors are used.

3.2.2 Onboard electronics

One goal of the STERN program is to include a telemetry downlink from the rocket to a ground station. This was realized with a commercially available flight computer named TeleMega, which is used mainly for high power model rocketry. This flight computer measures the rocket acceleration in 3 axes, flight attitude, and altitude with a set of acceleration, gyro, and pressure sensors. Additionally, it sends the GPS (global positioning system) position. A redundant configuration of two flight computers send their position data to a ground station. The most important task of the flight computers, as already mentioned previously, is the ejection of the drogue parachutes at the apogee as well as the main parachute near the ground. Figure 9 shows the wiring of one TeleMega, the pyrocutters for parachute deployment as well as the power supply. The second, redundant Telemega is not shown for better visibility. Additionally, a satellite

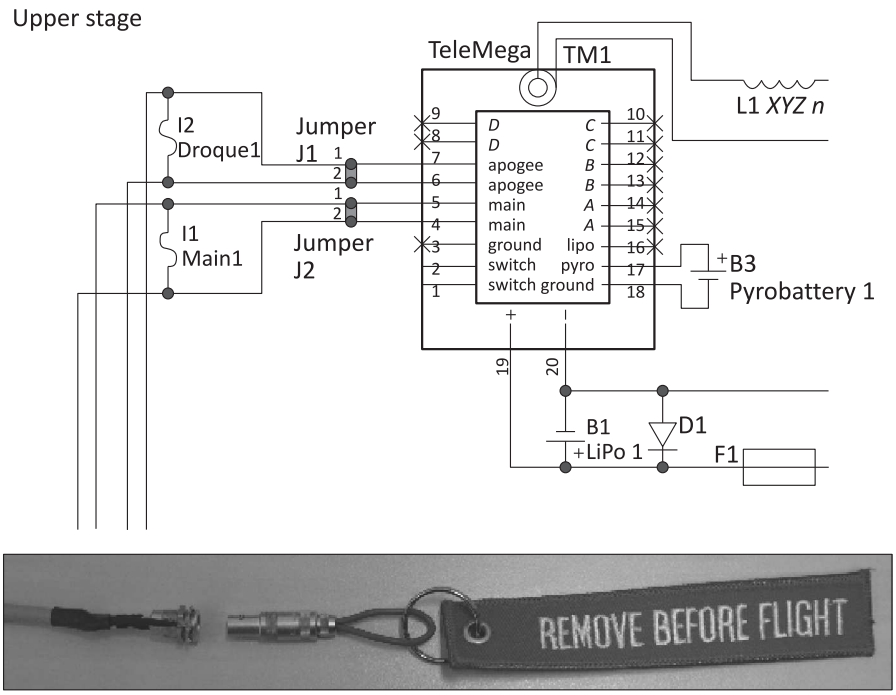

Figure 9 The S/A-device (Jumpers J1 and J2) within the rocket wiring diagram

tracking device called Spot Gen3 will be on board, which provides an additional GPS position via the Globalstar satellite network. This system will be used to locate the rocket on ground. A measurement system based around the Arduino microcontroller will measure the tank and engine pressure during the flight for postflight analysis.

3.3 HEROS Structure

In order to reduce the dry mass, the primary structure of the rocket consists of CFRP tubes which are produced using the fiber winding process. The orientation and thickness of the laminate layers were customized to withstand the occurring loads during the burn and recovery phases. The laminate has an overall thickness of 1.8 mm at an inner diameter of 220 mm. Buckling in the recovery phase is considered as the design parameter. The laminate is also optimized for the use of bolt connections that are needed to join the rocket parts. Connector tubes are used to conduct bending moments between sections to prevent the bolts

from getting asymmetrically loaded over the circumference of the rocket's body. Aluminum rings are fitted inside the connector tubes for screwing in external radial screws. As a result, a relatively small amount of screws is needed for the assembly which decreases the failure probability due to hole bearing or due to contact pressure in the CFRP. The fins of the rocket will be produced with CFRP in the sandwich construction type which leads to highly lightweight but also stiff structures. The fins will be directly laminated with CFRP on the hull segments.

4 HEROS PERFORMANCE AND FLIGHT SIMULATIONS

The goal of HyEnD at the beginning of the STERN program was to set the new altitude record for student rockets in Europe which at this point is at about 21 km held by the Stratos II rocket of TU Delft. HEROS was designed to reach at least an altitude of 20 km. During development of the propulsion system, the design of the rocket went through several iterations. By narrowing down uncertainties

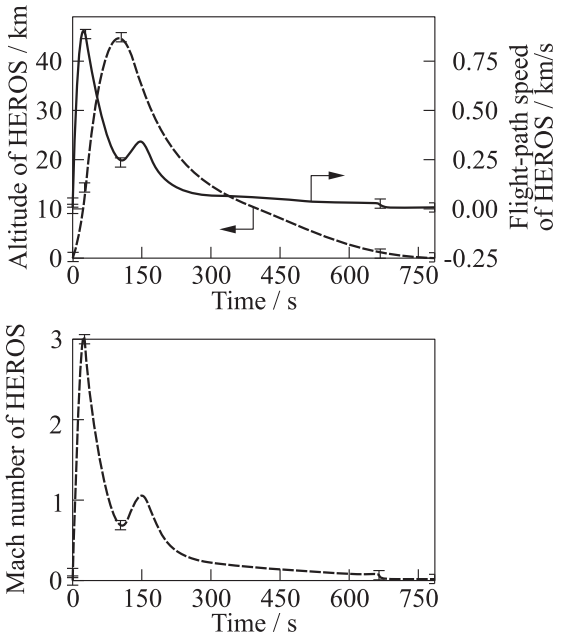

Figure 10 Altitude, flight-path speed, and Mach number vs. time

in the course of the development, maximizing the efficiencies and performance parameters, it was possible to increase the maximum flight altitude of HEROS up to 55 km, assuming the best case. Since all propulsion system components are prototypes, not everything is in an optimal state concerning lightweight or performance. As the flight campaign of HEROS is coming closer, a realistic estimation of the flight altitude of 35 to 45 km with the current mass balance of HEROS has been established. The total dry mass of the rocket is expected to be less than 75 kg while a total of about 100 kg of propellant will be loaded. The trajectory of HEROS is simulated with ASTOS, which is kindly provided by ASTOS Solutions for the STERN project. Figure 10 shows the nominal flight trajectory for HEROS in its current stage of development with a dry mass of 75 kg. The flight altitude in this case is about 45 km and the maximum Mach number is higher than 3.

5 ROCKET ENGINE TEST BENCH AND DATA ANALYSIS

5.1 Test Bench M11.5

The experimental tests with an engine of this thrust size are needed to be done in a safe and adequate environment. Therefore, a collaboration with the DLR Institute of Space Propulsion in Lampoldshausen was started for the test campaign. In 2012, the DLR Lampoldshausen started the design and construction of a new test bench M11.5 (Fig. 11). It is especially dedicated to support educational tests with students, hybrid rocket propulsion at larger scale, and new propellant combinations. It is an extension of the test complex M11 of the Department of Propellants.

Two test positions are available for experimental setups in mobile containers. This allows student teams to assemble their experiment in a container with mea-

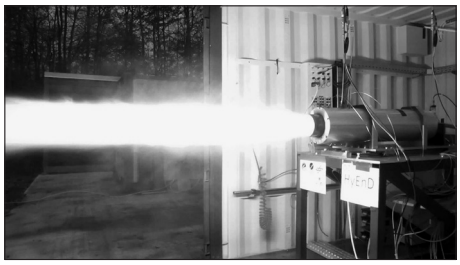

Figure 11 HyRES test at DLR Lampoldshausen test site M11.5

surements and instrumentation at their university and then bring the container for the test campaign to M11.5. Here, two supply lines for N_2O can be used for mass flow rates up to 5 kg/s. Additionally, several connections for N_2 auxiliary gas are installed at different pressure levels. The whole N_2O and N_2 supply is installed at M11.5 in secure distance from the containers behind concrete walls. The media supply and test campaigns are run from a dedicated control room. Several computer positions are available for the control of a test run by the DLR. Several network connections and remote video surveillance complete the testing capabilities. The test bench is also used regularly for student workshops for the DLR STERN program, for Summer school events, or for School Lab activities from the DLR Lampoldshausen, in order to provide hands-on experience for students during their education.

The measurement system consists of a National Instruments PXI system with different measurement cards for the respective sensors. The software was developed and programmed with Labview. The complete measurement system is installed separately in the rear part of the test container in order to provide short cable lengths and adequate safety from the engine testing. The tests are conducted remote controlled from the M11.5 control room in safe distance from the test site. More details about the sensors and their accuracies are given in [3, 30].

The test sequence is controlled remotely and executed via a National Instruments LabVIEW interface. The order and timing of operations are preprogrammed into an automated test fire sequence, thus ensuring a repeatable testing procedure. Burn times are set for each test based on the expected regression rate and initial port diameter of the fuel grain. About 4 s before the opening of the oxidizer valve, the N_2O tank gets pressurized. Igniter firing occurs 0.5 s before the opening of the oxidizer valve. The oxidizer valve is closed after the scheduled burning time and the lines and the chamber are purged with N_2.

5.2 Combustion Tests Analysis

5.2.1 Regression rate and performance analysis

Due to the two-phase propellant configuration, hybrid systems are characterized by a combustion limited by diffusion. This makes the fuel regression rate and the performance primarily dependent on the fluid dynamics in the combustion chamber and on the oxidizer mass flux which is changing during the combustion process. For this reason, hybrids are characterized by time-varying regression rate and performance. The aim of the regression rate analysis is to experimentally determine the ballistic coefficients for each fuel and oxidizer combination. Due to the discrete nature of fuel mass measurements, averaging both in space and time is necessary. Unfortunately, the methods of data reduction are not

unique because of the nonlinear nature of the problem and each method produces significantly different results. In this analysis, the space-time averaged regression rate as defined by Karabeyoglu *et al.* [31] was used. It produces the smallest averaging induced error. An error analysis was conducted in order to quantify the uncertainties in the computed variables associated with the regression rate measurements. The methods have been used which are described by Karabeyoglu *et al.* [31].

For the efficiency computation, the average performance was compared with theoretical values obtained with the software NASA CEA (Chemical Equilibrium with Applications), evaluated at the average chamber pressure $\overline{P}_c$ and oxidizer-to-fuel ratio by setting equilibrium conditions. An expansion ratio of 5 was used in the computations. More details are given in [3].

5.2.2 Frequency analysis

In order to better understand what happens in the combustion chamber during the burning process, a spectral analysis of the chamber pressure was carried out with MATLAB® using the Signal Processing Toolbox. Pressure data were windowed through a rectangular or Hanning window with the purpose of minimizing the spectral leakage for the calculation of the spectra over the entire firing. Then, a fast Fourier transform (FFT) was performed to display the overall spectrum. In order to reduce the noise, a moving average and an autospectrum were performed for each test. A Power Spectral Density, using the MATLAB "Pwelch" routine, was also applied to the pressure data. A spectrogram was used to get a better overview of the frequencies resolved over time.

5.3 Combustion Instability

From a general point of view, smooth combustion occurs when pressure oscillations during steady operation do not exceed ±5% of the mean chamber pressure. Combustion that gives greater pressure fluctuations which occur at random intervals is called rough combustion. Combustion is defined to be unstable when the fluctuations in the chamber pressure exceed more than ±5%–10% of the mean pressure value and it is characterized by oscillations occurring at well-defined time intervals [32]. These oscillations cause an energy transfer from the combustion to the acoustic modes of the chamber, which lead to different failure mechanisms due to the increase in chamber pressure or heat transfer to the walls. Fortunately, the combustion chamber pressure oscillations observed in hybrid systems are normally limited in amplitude and typically are not able to produce catastrophic consequences. This is most likely due to the nonpremixed diffusion controlled flame which makes the regression rate not pressure depen-

dent. However, oscillatory combustion in hybrids still generates high structural loads, thermal loads, thrust oscillations, and high regression rates (direct-current shift) which lead to unplanned thinning of the fuel web and the insulation material. From a general point of view, strong instabilities have to be avoided because they cause excessive mechanical vibrations on the structure; on the other hand, mild instabilities may improve combustion efficiency by promoting mixing between fuel and oxidizer. Combustion instabilities in hybrid rocket engines are classified into the following categories:

– **nonacoustic instabilities**: they are usually characterized by low-frequency chamber pressure fluctuations and low intensity. Typically, they are caused by a coupling between the oxidizer mass flow in the feed system and the combustion process, chuffing of the solid fuel, coupling between the atomization/vaporization lags of the liquid oxidizer and the combustion and gasdynamic processes in the chamber, and pressure sensitivity of the combustion (only at very high and low oxidizer mass flux regimes). The typical nonacoustic combustion instabilities for hybrids are called intrinsic low-frequency instabilities which are associated with the boundary layer combustion process. They are observed for both liquid and gaseous oxidizers. According to Karabeyoglu *et al.* [33], these instabilities are based on a complex coupling between thermal transients in the solid fuel, wall heat transfer blocking, and the transients in the boundary layer. The empirical formula for this frequency is [33]:

$$f_{\mathrm{ILF}} = \frac{0.48}{\tau_{\mathrm{bl}}} = 0.2341 \left(2 + \frac{1}{\mathrm{OF}}\right) \frac{G_{\mathrm{Ox}}(RT)_{\mathrm{av}}}{L_{\mathrm{fuel}} P_c} \,.$$

Vortex-shedding can appear in the pre- or postcombustion chamber. It produces combustion instability if its frequency matches with the frequency of an acoustic mode. Carmicino [34] gives two relations for computing the frequency of the vortex shedding instabilities in the pre- and postcombustion chamber for a cylindrical fuel sample with a single central port perforation:

$$f_{\text{VS-pre}} = \mathrm{Sr} \frac{4\dot{m}_{\mathrm{Ox}} R_{\mathrm{Ox}} T_{\mathrm{Ox}}}{\pi D_f^3 P_c} \,;$$

$$f_{\text{VS-post}} = \eta_{c^*} c^*_{\mathrm{th}} \psi^2_{\mathrm{th}} \mathrm{Sr} \, \frac{D_t^2}{D_f^3} \,;$$

– **acoustic instabilities**: these oscillations are characterized by higher frequencies and amplitudes with respect to the nonacoustic ones. They often coexist or are believed to be triggered by the low-frequency instabilities. Typical acoustic modes are the Helmholtz frequency f_H, also known as the bulk mode, which is related with the gas motion in and out of the

nozzle, and the first longitudinal acoustic frequency f_{1L} of the chamber. According to Carmicino [34], they are defined as

$$f_H = \frac{c}{2\pi}\sqrt{\frac{A_t}{V(l+0.8D_t)}}\,;$$

$$f_{1L} = \frac{c}{2L} = \sqrt{\frac{\gamma(RT)_{\text{av}}}{2L}}\,.$$

6 MIRAS SMALL-SCALE DEMONSTRATOR TESTS

A test campaign of 89 hot fire ground tests was carried out during the months from September 2013 to July 2014 at the test bench M11.5 at DLR Lampoldshausen. Cylindrical paraffin-based fuel samples with a single central port perforation were tested in combination with N_2O. The chamber pressure was about 30–35 bar and the expansion ratio of the engine was 5.

6.1 Propellant Characteristics

The fuels used for the test campaign are four different paraffin waxes, both in pure form and with additives in order to modify mechanical, rheological, and burning properties. Their properties are reported in [25]. Types 6003 and 6805 are the pure paraffin waxes. Type 0907 is a microcrystalline wax. Type 1276 is a formulation based on waxes and different additives inserted by the manufacturer in order to increase the mechanical properties of the pure paraffin [35, 36].

For the ballistic tests, all the samples were blackened in order to limit radiation effects into the fuel during combustion. Generally, the amount of blackening additive was about 1% so that it has a negligible impact on the performance. Four different additives were chosen to improve the mechanical properties of the paraffin samples. Stearic acid (SA) was used in combination with paraffin 6003 and 6805. A nanoclay material from the manufacturer Byk and two polymers with a melting temperature similar to the paraffin samples were used in combination with 6805 [25]. The oxidizer used for the test campaigns is N_2O commonly known as laughing gas. It is used as oxidizer in rocket engines because it is nontoxic, storable, and nonexplosive at room temperature, self-pressurizing with a high vapor pressure, relatively safe and easy to handle [8, 11, 37, 38]. The self-pressurization allows for a simple oxidizer feed system with no additional pressurizing gas or even pumps.

6.2 MIRAS Test Setup

Two different rocket engines were used during the experimental campaign of the small-scale MIRAS demonstrator.

The main combustion chamber for both engines consists of a cylindrical aluminum central section and aluminum flanges at the end. The central body has an outer diameter of 75 mm and a length of 145 mm. The whole chamber has a length of 22 and 27 cm, respectively, for the first and second engines (Fig. 12) and both deliver a thrust of about 500 N and a burning time of about 5 s. The chamber pressure is approximately 30 bar and the selected oxidizer to fuel ratio O/F lies around 5–7. The whole combustion chambers are made of aluminum, which has high strength and corrosion resistance. The interior of the aluminum casing is protected from the hot combustion gases of up to 3000 K by an ablative layer of PERTINAX, a composite material from paper and a phenol-formaldehyde synthetic resin, which is capable to withstand high temperatures for some seconds. Both test articles have a convergent-divergent graphite nozzle with an expansion ratio of about 5 and a conic shape. Several diaphragms with different geometries were used during the test campaign in both engine config-

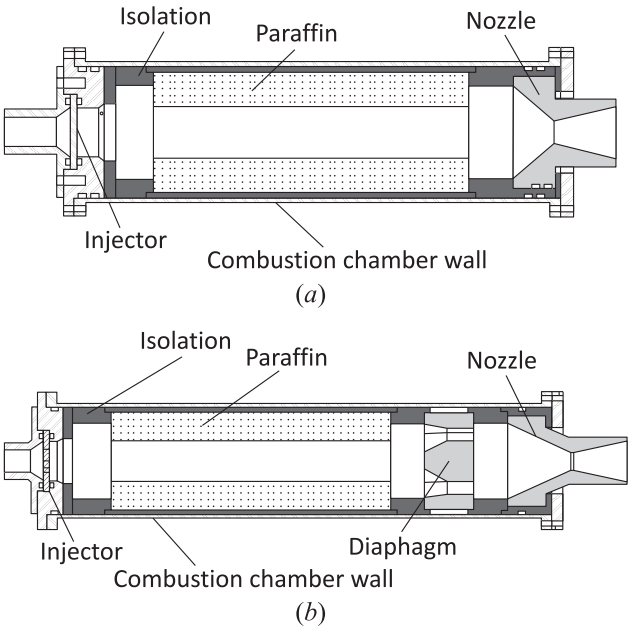

Figure 12 Cross sections of the small-scale 500-newton test articles: (*a*) first version; and (*b*) second version

Table 6 Overview of injectors used during the experimental campaign

Injector	2α	$L_{\text{inj}}/D_{\text{inj}}$	Inclined holes	Straight holes
Axial showerhead No. 1	0°	6	0	48
Axial showerhead No. 2	0°	6	0	42
Axial showerhead No. 3	0°	6	0	20
Axial showerhead No. 4	0°	3	0	22
Impingement No. 1	30°	4.5	10	0
Impingement No. 2	30°	6	16	0
Swirl + Axial	0°	3 (Swirl) / 3.15 (Axial)	3	8

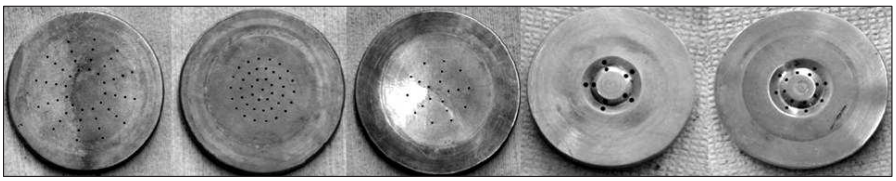

Figure 13 Injectors from left to right: axial showerheads No. 1, No. 2, and No. 3 and impingement injector No. 1 and No. 2

urations. They were placed at the end of the fuel grain to improve the mixing of the propellants and, thereby, increase the combustion efficiency. The ignition system is an electrically-initiated pyrotechnic igniter.

The stability of a hybrid rocket engine is closely linked to the injectors geometry and to the configuration of the precombustion chamber. In this research, different kinds of injectors were used as listed in Table 6. The axial showerhead injectors and the impingement injectors are shown in Fig. 13.

6.3 MIRAS Test Results

6.3.1 Regression rate analysis

Experimental data of single tests were analyzed as explained in subsection 5.2. The space–time averaged regression rates and oxidizer mass fluxes were computed, together with the error bars for the regression rate. Then, the regression rate curves for each paraffin formulation were plotted by using a power law interpolation of the single tests. The curves for the tested fuel formulations with showerhead injectors are shown in Fig. 14. Literature data of

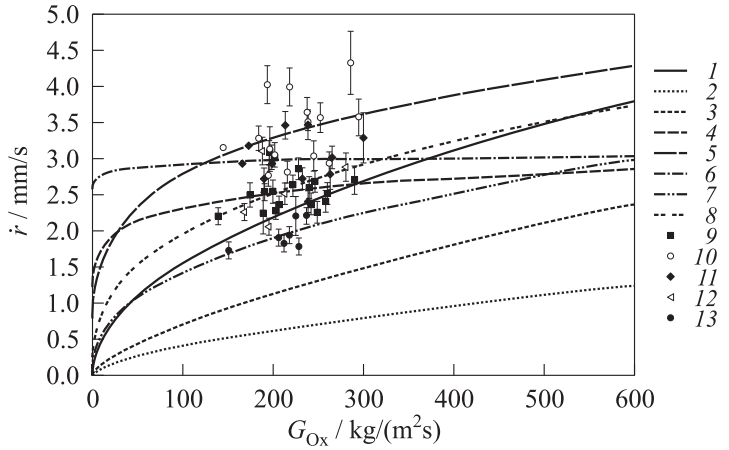

Figure 14 Regression rate curves: *1* — N_2O/SP-1a; *2* — LOx/HDPE (Stanford); *3* — LOx/HTPB (ATK data); *4* — N_2O/0907; *5* — N_2O/6003–10% SA; *6* — N_2O/6805–10% SA; *7* — N_2O/6805–5% Polymer2; *8* — N_2O/6805–5% Polymer1–2% CL; *9* — 0907; *10* — 6003/10% SA; *11* — 6805/10% SA; *12* — 6805/5% Polymer1/2% CL; *13* — 6805/5% Polymer2

HTPB, high-density polyethylene (HDPE), and another paraffin-based fuel in combination with different oxidizers are also shown in order to compare the results.

Details of the tests data are given in Table 7.

It is possible to note that all the fuel formulations tested during the test campaign in combination with N_2O show a regression rate that is higher than that of polymeric fuels in combination with LOx. This is due to the additional mass transfer caused by the entrainment which leads to an increase in the fuel surface roughness and to a reduction of the effective heat of gasification and blocking factor in the boundary layer. Moreover, it is possible to see that tests performed with paraffin 6003 and 6805 both with 10% of stearic acid show the highest regression rates. They also have the lowest viscosity which means a higher mass flow is entrained from the fuel surface. In fact, the regression rates are decreasing as the viscosity values of the fuel samples are increasing as it was shown in detail [25]. The viscosity data measurements of these paraffin formulations are also shown in [25]. The mixture with 5% of polymer show a regression rate which is lower with respect to that of other paraffin-based mixtures but still higher than that of polymeric fuels.

Table 6 shows different injectors that were tested. Note that impingements 1 and 2 have the same holes area but different number of holes. If the injector is changed from the axial to the impingement 1, a strong increase of the regression

Table 7 The 500-newton engine test matrix (averaged values)

Test No.	Fuel	P_c, bar	O/F	G_{Ox}, kg/(m^{2}s)	$\dot{r}_f$, mm/s
2	0907	32	5.2	137.6	2.2
3	0907	29.8	6	188.5	2.25
5	0907	36.7	7.4	203	2.27
6	0907	38	5.7	190.1	2.54
	6003 + 10% SA	37	5.6	194.5	2.76
11	6805 + 10% SA	30.7	6.3	264.2	3
12	6805 + 10% SA	31.4	5.3	190	2.73
13	6805 + 10% SA	35	4.7	212.4	3.45
14	6003 + 10% SA	33.7	6.6	261.7	2.94
15	6003 + 10% SA	38.2	5.4	251.6	3.57
16	0907	32.5	8.6	248.4	2.25
17	0907	33.6	8	241.1	2.37
18	0907	31	7.4	259.7	2.51
19	0907	33.3	6	221.7	2.63
20	6805 + 10% SA	30.5	5.3	198.3	2.92
21	6003 + 10% SA	31.8	5.2	201.2	3
22	0907	33.6	6	227.3	2.85
23	6003 + 10% SA	33.4	5	197.3	3.11
24	6003 + 10% SA	33.6	4.5	183.2	3.27
25	0907	33	5.1	199.8	3
26	0907	35	6.6	245.6	2.67
27	0907	33.3	5.8	198.5	2.54
28	0907	35.4	6.9	206.2	2.35
29	0907	35	6.4	240.8	2.60
30	6805 + 10% SA	32.5	6.1	231	2.71
31	6003 + 10% SA	33.3	4.4	284.7	4.32
32	6003 + 10% SA	34.5	5.7	215	2.81
36	0907	31.7	7.6	257.3	2.40
37	6003 + 10% SA	34.3	5.8	295.6	3.57
39	6003 + 10% SA	34.7	5.1	238	3.50
40	6805 + 10% SA	32.5	7.2	238.2	2.40
41	6805 + 10% SA	28.2	6.7	262.6	2.78
42	6805 + 10% SA	27.2	4	165.2	2.93
43	0907	31	7.1	290	2.71
44	0907	26.1	4.8	173.9	2.48
45	6805 + 10% SA	34.2	3.8	179.3	3.78
46	6003 + 10% SA	25.6	3.4	144.5	3.14
47	0907	32.7	4.5	182	3.21
49	6805 + 10% SA	28.7	5.7	299	3.27
50	6805 + 10% SA	38.1	4	179.8	3.58
51	6003 + 10% SA	27.3	5.4	244.5	3

To be continued on p. 53

Table 7 (*continued*) The 500-newton engine test matrix (averaged values)

Test No.	Fuel	P_c, bar	O/F	G_{Ox}, kg/(m^{2}s)	$\dot{r}_f$, mm/s
52	6003 + 10% SA	35.4	3.6	192.8	4
54	6805 + 10% SA	33.7	3.3	160.8	3.86
55	6003 + 10% SA	29.7	4.7	237.6	3.64
56	6805 + 10% SA	34.4	3	175.1	4.37
57	6003 + 10% SA	27.2	4	218.1	3.97
58	6805 + 10% SA	34.6	3	181.6	4.44
59	6805 + 10% SA	30.7	5	218.1	3.10
60	0907	26	4.7	196.4	3.10
61	6805 + 10% SA	31.4	4.7	221.2	3.12
63	6805 + 10% SA	28.5	4.7	167.2	2.65
67	6805 + 10% SA	34.3	5.2	172	2.55
70	6805 + 5% pol1 + 2% CL	26.5	6.4	281.6	2.87
72	6805 + 5% pol1 + 2% CL	27	5.7	212.1	2.52
74	6805 + 5% pol1 + 2% CL	25	5.2	168	2.25
76	6805 + 5% pol1 + 2% CL	24.5	6.8	195	2.06
78	6805 + 5% pol1 + 2% CL	27.5	4.4	187	3.10
79	6805 + 5% pol2	22	7.5	217.8	1.94
80	6805 + 5% pol2	28.4	7.3	237.2	2.20
81	6805 + 5% pol2	20.2	6	224.8	2.20
82	6805 + 5% pol2	18	5.9	150.6	1.72
83	6805 + 5% pol2	33.6	7.5	205.9	1.91
85	6805 + 5% pol2	32	7.6	211.6	1.82
86	6805 + 5% pol2	35.4	8.7	227.8	1.78

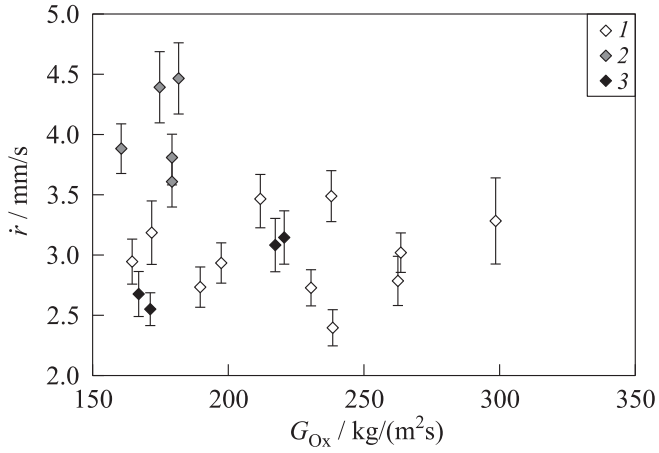

Figure 15 Regression rate curves with axial (*1*) and impingement (*2* and *3*) injectors (6805 + 10% SA)

rate is seen. This is due to a more uneven distribution of the oxidizer and to an increase in the local N_2O impinging on the fuel surface. The space-time averaged regression rate values for the mixture 6805 + 10% SA with axial and two different impingement injectors are shown in Fig. 15.

It is important to note that configurations with and without diaphragm show the same regression rate since it is placed at the end of the fuel grain.

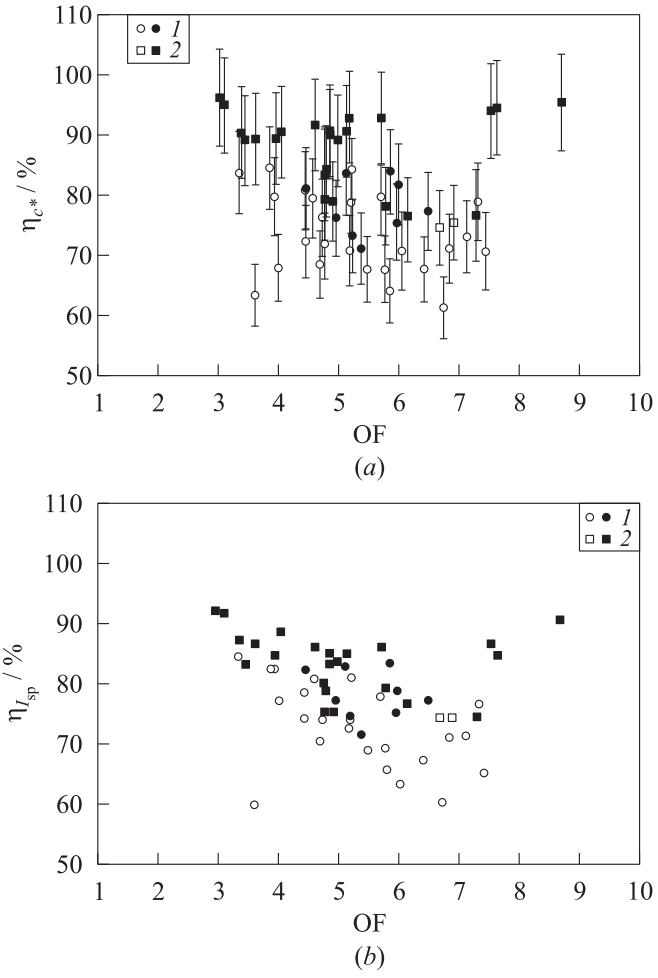

Figure 16 Efficiency of characteristic velocity (*a*) and specific impulse (*b*) vs. mixture ratio: engine 1 (*1*); and engine 2 (*2*) without (blank symbols) and with diaphragm (filled symbols)

6.3.2 Engine Performance Analysis

Average engine c^* efficiencies and their error bars are computed as explained in subsection 5.2 and are reported in Fig. 16*a*. Higher combustion efficiencies are reached using the engine with the longer postcombustion chamber, since it enhances the mixing of the combustion products and increases the residence time. In order to reach a more complete mixing without increasing too much the engine volume and dry mass, the postcombustion chamber was used in combination with a perforated mixing plate located at the end of the fuel grain. Different diaphragm geometries were tested in both engines and an increase in the combustion efficiency with respect to configurations without diaphragms was observed. This happens because the diaphragm forces the mixing of the oxidizer with the fuel and combustion products generated before it, thus enhancing the local completeness of the combustion [39]. The price of a higher c^* efficiency is a pressure drop across the diaphragm that reduces the chamber pressure available for the expansion in the nozzle. Moreover, higher combustion efficiencies are reached with the impingement injector due to a better atomization of the oxidizer. Finally, the combustion efficiency tends to increase with decreasing mixture ratio since with fuel-rich conditions, a more complete combustion of the oxidizer is accomplished. The efficiencies of the specific impulse in Fig. 16*b* show the same trend as the combustion efficiencies.

6.3.3 Combustion stability analysis

A frequency analysis of the chamber pressure signal was performed with MATLAB® using the Signal Processing Toolbox. Combustion stability was evaluated by using FFT, spectrograms, and "Pwelch" plots. All the theoretical frequencies were computed using the formula given by Karabeyoglu *et al.* [33] and Carmicino [34] (see subsection 5.2). They are compared with the experimental frequencies magnitude peaks from the plots.

In general, the intrinsic low-frequency instability was present in most tests even if the oscillations were never so high to cause an unstable burning behavior. It varies in a range that goes from 70 to 140 Hz depending on the injector geometry and on the presence of the diaphragm. In some tests, a peak in correspondence of the vortex shedding frequency in the prechamber is shown. Its theoretical value lies between 30 and 90 Hz. The first longitudinal frequency, which is around 2500 Hz for the smaller chamber and 2000 Hz for the longer one, could not be measured with the instrumentation used for the majority of the tests since the pressure sensor had a sampling frequency of 1000 Hz.

From the experimental data, it is possible to note that no strong instabilities were observed during the tests in general. The oscillations of the chamber pressure remained bounded in a range from less than 1% up to 9% of the mean

pressure value. The highest oscillations are associated with the presence of the diaphragm at the end of the fuel grain and injectors with improper atomization behavior. Lower oscillations are observed for tests without the diaphragm and with the impingement injector. In particular, it is possible to note that tests using an impingement injector show a very stable combustion with oscillations lower than 1%, also in presence of a diaphragm. For example, tests using 6805 + 10% SA showed oscillations of almost 9% for the configuration with the diaphragm and the 48-hole axial injector, while they were 0.8% for the configuration with the diaphragm and the impingement injector. This is most likely due to the improved atomization behavior of impingement injector with respect to the axial one. Moreover, oscillations also depend on the conditions of the oxidizer. From the results of other tests, it was seen that the stability is improved by a high vapor pressure of the N_2O in the combustion chamber. In fact, when the local pressure in the chamber is below the vapor pressure, N_2O is expected to flash vaporize.

Tests 36 and 86 were performed under comparable operating conditions but different injector configurations. In test 36, the axial showerhead injector No. 2 was used while in test 86, it was replaced by the impingement injector No. 2. The chamber pressure time traces, spectrograms, and FFT are seen, respectively, in Figs. 17, 18, and 19.

Test 36 shows chamber pressure oscillations with an amplitude of approximately 5.4% of the mean pressure. It is possible to note a typical feed system coupled instability behavior with strong oscillations also upstream of the injector and in the chamber, at about 100 Hz. This instability arises mostly due to a low injector pressure drop. At the end of the combustion, the nozzle cracked and increased the effective throat diameter. This caused a decrease in the chamber pressure and an increase in the injector pressure drop, thus leading to a sta-

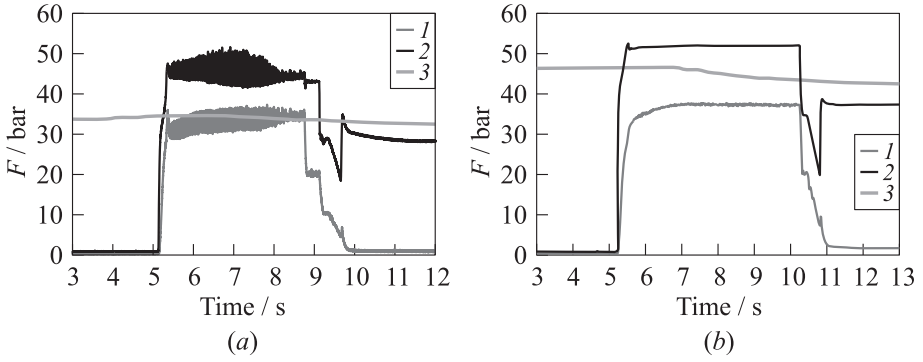

Figure 17 Pressure–time trace tests 36 (*a*) and 86 (*b*): *1* — chamber pressure; *2* — injection pressure; and *3* — vapor pressure

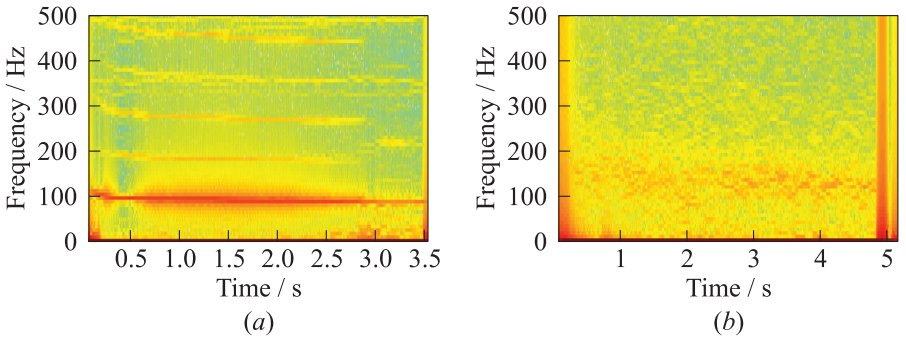

Figure 18 Chamber pressure spectrogram tests 36 (*a*) and 86 (*b*)

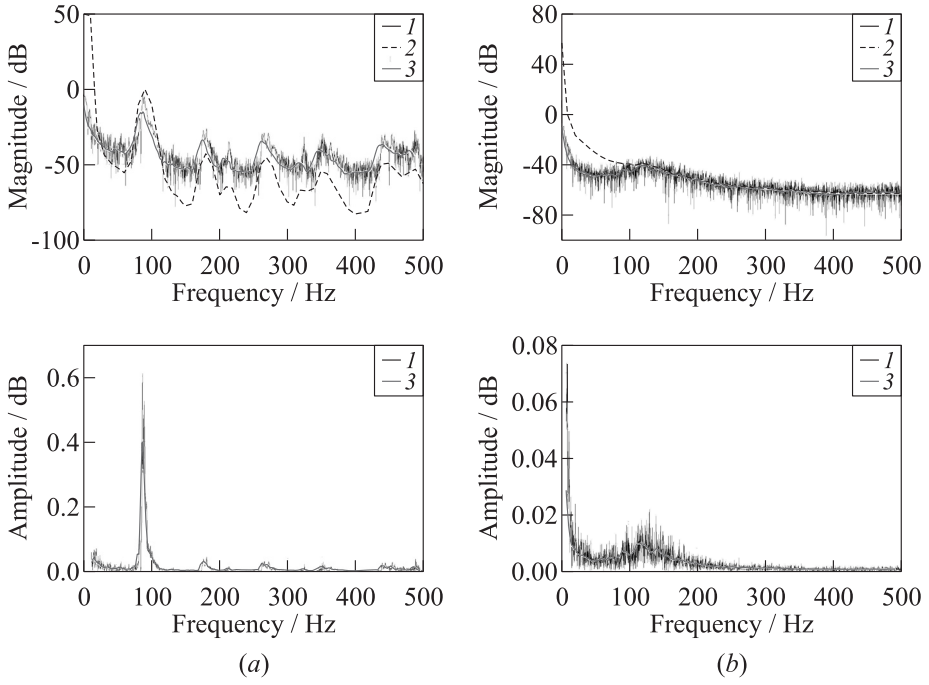

Figure 19 Chamber pressure spectrum tests 36 (*a*) and 86 (*b*): *1* — spectrum; *2* — autospectrum; and *3* — moving average

ble combustion. In the spectrogram, strong oscillations at about 100 Hz are clearly seen, together with other oscillations at around 200 and 300 Hz which are the second and the third modes of this instability. Lower frequency oscillations, associated with the vortex shedding in the prechamber, are present at around 50 Hz at the beginning of the combustion. The oscillations between 350 and 400 Hz, which are present during the entire burning process, are linked to the Helmholtz mode. An oscillating band with decreasing frequency, associated with the vortex shedding in the postchamber, are seen between 500 and 450 Hz. It is not possible to see the acoustic modes due to the low sampling frequency of the pressure transducer. In contrast to that, test 86 shows a stable combustion without strong oscillations. In the spectrogram, only a low-intensity oscillating band at about 100 Hz is seen, which is in the range of the low-frequency instability. Test 86 shows stable performance due to the improved atomization behavior of the impingement injector and due to a 20 percent higher pressure drop over the injector.

7 HyRES ROCKET ENGINE TEST RESULTS

The time for the HyRES engine development and the test campaign was rather limited, due to the short overall project time frame. Therefore, an extensive test campaign was realized with the subscale 500-newton hybrid rocket engine. This enabled a high number of tests at low cost and a short time between two tests. Currently, 89 tests have been performed with this engine, including one flight demonstration with the MIRAS rocket. Several important results were achieved which were used directly for the design of the scaled-up HyRES engine. The tests were done at the same test facility and, if possible, under similar operating conditions as in the 10-kilonewton tests. Thanks to these tests, many optimizations have been incorporated already into the first design of the HyRES engine.

Some of the most important results include the characterization of a wide number of different paraffin-based fuels. Their regression rate was characterized by their liquid viscosity [25]. The mechanical strength was optimized as well. Special care was taken concerning the stability of the combustion process. Combustion instability lowers the performance and increases the loads on the rocket structure and payload. In general, the injector and precombustion chamber configuration determine the stability of the motor. The postcombustion chamber is used to optimize the efficiency of the engine. Several different injectors were tested and their effect on efficiency was determined, as shown in the previous section. Good and rapid atomization and vaporization of N_2O was crucial for the stability as well as the efficiency of the engine. An injector with proper atomization of the oxidizer and sufficient pressure drop was needed to avoid feed

Table 8 The HyRES test matrix

Test No.	Configuration	Time, s	Comments
i-0	Igniter test	2	
0	N_2O cold flow, 5-kilonewton injector	3	
1	5-kilonewton injector	5	
2	5-kilonewton injector	5	Ignition improved
3	5-kilonewton injector	10	Thermal design test
4	5-kilonewton injector	5	Increased efficiency
5	10-kilonewton injector, reduced chamber pressure	5	
6	10-kilonewton injector, full pressure and thrust	5	Design conditions
7	10-kilonewton injector, full pressure and thrust	3	Design conditions
8	10-kilonewton injector, full pressure and thrust	12	Facility upgrade

system coupled instabilities. It was found that the precombustion chamber configuration needs to be designed in a good way such that flame anchoring and a continuous recirculation zone are established. Also, the sudden formation of large vortices with too much unburned propellants needs to be avoided. The postcombustion chamber was optimized to provide better mixing of the propellants and enable a high c^* efficiency. It was seen that a considerable pressure drop is measured between the pressure measurement of the pre- and postcombustion chamber. This must be taken into account carefully when evaluating the engine efficiencies and performance. All this summarized knowledge enabled the successful design of this large-scale engine in a very short number of tests which also minimized greatly the overall costs.

The test matrix of the HyRES test campaign is shown in Table 8. Eight tests were done currently. The performance of the engine and the operation of the test bench were gradually increased during the campaign. The first two tests showed a small initial drop in chamber pressure. This was identified to be caused by a too small pyrotechnical ignition charge and, thereby, was improved for the later tests. Test number 3 was done for 10-second burn time to verify the thermal design of the engine. A modification in the postcombustion chamber was introduced in test 4 to increase the c^* efficiency. As a next step, the full mass flow injector was used for test 5 and later tests. During tests 6 and 7, the engine was operated for the first time at its design conditions. The latest test 8 was at the design condition of the engine for a burn time of 12 s. This was realized with the latest upgrade of the M11.5 test facility with a 250-liter volume N_2O run tank. The previous tests were limited in burn time due to a smaller tank.

Figure 20 shows the pressure and thrust measurements for test 8. In Fig. 20*a*, P_{cc1} and P_{cc2} are the measured pressures in the pre- and postcombustion cham-

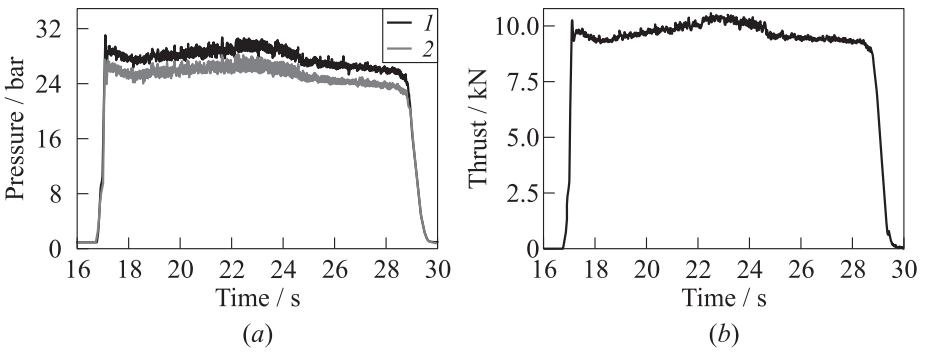

Figure 20 The HyRES pressure (*1* — p_{cc1} and *2* — p_{cc2}) (*a*) and thrust measurement (*b*) of test 8

ber, respectively. The filtered thrust measurement signal is shown in Fig. 20*b*. Both pressure and thrust show a steady-state behavior. The combustion chamber pressure signals are stable with very little oscillations.

8 CONCLUDING REMARKS

HyEnD is developing an experimental hybrid sounding rocket called HEROS, which is planned to be launched to an altitude of 40 to 50 km at Esrange in Kiruna in October 2015. This is done within the STERN educational program of the DLR which enables student groups at several German universities to develop and launch their sounding rockets. HEROS will be propelled by a 10-kilonewton hybrid rocket engine called HyRES, using paraffin-based fuel and self-pressurizing N_2O as oxidizer. The design and performance of HyRES and its fuel were optimized in a 2-step test campaign at the test bench M11.5 at the DLR Lampoldshausen. A small-scale 500-newton demonstrator engine, called MIRAS, was used to gather experience and better understanding of the underlying physical combustion processes. This approach enabled a high number of tests at small scale and low cost. The most important design goals and test results were achieved successfully, which means a stable combustion at high efficiency.

To maximize the possible flight altitude of HEROS, a lot of efforts have been put into lightweight components. A major task was to develop an oxidizer tank with a volume of more than 100 l and a dry mass below 30 kg. A CFRP tank with an aluminum liner, to guarantee compatibility to N_2O, was developed and manufactured.

Another important development of the propulsion system was the pyrotechnically actuated valve, which compared to off-the-shelve valves of comparable

volume and mass flow, is very lightweight with less than 1 kg of mass. The recovery system is a major subsystem next to the propulsion system. The structural parts are designed to sustain the lightweight concept of HEROS. The rocket hull and the fins are constructed using CFRP. These features allow HEROS to reach a top speed above Mach 3, a flight altitude of up to 50 km, and a full recovery for reusability of the whole rocket if all goals are reached during the launch campaign.

The development, optimization and testing of both the 500-newton and the 10-kilonewton hybrid rocket engines are described in detail. A test campaign of 89 tests was carried out using the 500-newton engine and, up to now, 8 tests were performed with the 10-kilonewton engine. The MIRAS test campaign was targeted at the effects of the fuel composition, the injector configuration, fluid dynamic effects, combustion stability, and efficiency. Regression rates and performance parameters of each test were computed by a time-averaging process over the burning time. Combustion stability was evaluated by using FFT, spectrograms, and power spectral densities of the chamber pressure signal. Different paraffin-based fuels show a decreased regression rate as their liquid viscosity is increasing. The regression rate is also influenced by the injector configuration. Engine configurations with a diaphragm placed at the end of the fuel grain do not show any increase in the regression rate. Concerning the engine performance, it was found that the combustion efficiency increases up to 25% when a diaphragm is placed at the end of the fuel grain due to the enhanced mixing of the propellants. No strong instabilities were observed during the tests, oscillations of the chamber pressure remain bounded in a range from less than 1% to 9% of the mean pressure value. The higher oscillations are associated with the presence of the diaphragm at the end of the fuel grain and injectors with poor atomization performance. Lower oscillations are observed for tests without the diaphragm and with the impingement injector, which promotes a better oxidizer atomization and propellant mixing. These results were used for the design of the 10-kilonewton scale-up engine. During the HyRES test campaign, the performance of the engine was gradually increased up to the design conditions. The most important design goals and test results were achieved successfully: a stable combustion at high efficiency and a delivered total impulse of more than 100 kN·s. This proves the applicability of this engine concept for the targeted launch date in October 2015.

ACKNOWLEDGMENTS

Since September 2012, the HyEnD-STERN project is sponsored by the DLR Space Administration with funding from the Federal Ministry for Economic Affairs and Energy (BMWI) at the Institute of Space Systems at the University

of Stuttgart, under the Grant No. 50RL1254. The experimental tests have been performed in cooperation with the Institute of Space Propulsion at the DLR Lampoldshausen, at the test complex M11.5. The support of the DLR Lampoldshausen and its Department of Propellants is greatly acknowledged. The authors would like to thank all the students, individuals, institutes, and companies who supported the presented work in several manners. Special thanks are to Dr. Thomas Wegmann at the Institute of Space Systems for his excellent administrative support. Further documentation and a complete list of our supporters are presented at www.hybrid-engine-development.de.

REFERENCES

1. Kobald, M., H. Moser, A. Bohr, and S. Mielke. 2009. Development and optimization of a hybrid rocket engine. *Deutscher Luft- und Raumfahrtkongress*. Aachen, Deutschland.
2. Lappoehn, K., D. Regenbrecht, and D. Bergmann. 2013. STERN — a rocket programme for German students. *5th European Conference for Aeronautics and Space Sciences*. Munich, Germany.
3. Petrarolo, A., M. Kobald, and C. Schmierer. 2015. Characterization of advanced hybrid rocket engines. *6th European Conference for Aeronautics and Space Sciences*. Krakow, Poland.
4. Schmierer, C., M. Kobald, K. Tomilin, U. Fischer, and M. Rehberger. 2015. HEROS — sounding rocket development by the HyEnD project. *6th European Conference for Aeronautics and Space Sciences*. Krakow, Poland.
5. Jones, M. D., T. M. Abel, and D. J. Weeks. 1997. Subscale hybrid rocket motor testing at the Marshall space flight center in support of the Hybrid Propulsion Demonstration Program (HPDP). AIAA Paper No. 1997-2800.
6. Park, O. Y., C. T. Bryant, and R. L. Carpenter. 2000. Performance analyses of HPDP 250K hybrids. AIAA Paper No. 2000-3544.
7. Dunn, Z., J. Dyer, K. Lohner, E. Doran, C. Bayart, A. Sadhwani, G. Zilliac, M. A. Karabeyoglu, and B. Cantwell. 2007. Test facility development for the 15,000 lb thrust peregrine hybrid sounding rocket. AIAA Paper No. 2007-5358.
8. Dyer, J., E. Doran, Z. Dunn, K. Lohner, C. Bayart, A. Sadhwani, G. Zilliac, B. Cantwell, and M. A. Karabeyoglu. 2007. Design and development of a 100 km nitrous oxide/paraffin hybrid rocket vehicle. AIAA Paper No. 2007-5362.
9. Dyer, J., G. Zilliac, E. Doran, M. T. Marzona, K. Lohner, E. Karlik, B. Cantwell, and M. A. Karabeyoglu. 2008. Status update report for the Peregrine 100km sounding rocket project. AIAA Paper No. 2008-4892.
10. Doran, E., J. Dyer, M. T. Marzona, M. A. Karabeyoglu, G. Zilliac, R. Mosher, and B. Cantwell. 2009. Status update report for the Peregrine sounding rocket project: Part III. *45th AIAA/ASME/ SAE/ASEE Joint Propulsion Conference and Exhibit*. Denver, CO.

11. Zilliac, G., B. Waxman, E. Doran, J. Dyer, and M. A. Karabeyoglu. 2012. Peregrine hybrid rocket motor ground test results. AIAA Paper No. 2012-4017.
12. Zilliac, G., B. S. Waxman, B. Evans, M. A. Karabeyoglu, and B. Cantwell. 2014. Peregrine hybrid rocket motor development. *50th AIAA/ASME/SAE/ASEE Joint Propulsion Conference*. Cleveland, OH.
13. Waxman, B. S., J. E. Zimmerman, B. J. Cantwell, and G. Zilliac. 2013. Mass flow rate and isolation characteristics of injectors for use with self-pressurizing oxidizers in hybrid rockets. *49th AIAA/ASME/ SAE/ASEE Joint Propulsion Conference*. San Jose, CA.
14. Zimmerman, J. E., B. S. Waxman, B. J. Cantwell, and G. Zilliac. 2013. Review and evaluation of models for self-pressurizing propellant tank dynamics. *49th AIAA/ASME/ SAE/ASEE Joint Propulsion Conference*. San Jose, CA.
15. Waxman, B. S., J. E. Zimmerman, B. J. Cantwell, and G. Zilliac. 2014. Effects of injector design on combustion stability in hybrid rockets using self-pressurizing oxidizers. *50th AIAA/ASME/SAE/ASEE Joint Propulsion Conference*. Cleveland, OH.
16. Karabeyoglu, M. A., J. Stevens, D. Geyzel, B. Cantwell, and D. Micheletti. 2011. High performance hybrid upper stage motor. AIAA Paper No. 2011-6025.
17. Micheletti, D., and M. A. Karabeyoglu. 2011. Paraffin-based hybrid rocket testing at the butte aerotec facility. *62nd Astronautical Congress (International)*. Cape Town, South Africa. IAC-11-C.4.3.6.
18. Knowles, T., D. Kearney, and R. Roberts. 2005. Overview of 10 inch diameter HTPB hybrid motor testing with liquid oxygen at Stennis Space Center. AIAA Paper No. 2005-4092.
19. Boardman, T. A., R. L. Carpenter, S. E. Claflin, B. E. Goldberg, and C. W. Shaeffer. 1993. JIRAD subscale hybrid rocket testing results. *Space Programs and Technologies Conference and Exhibit*. Huntsville, AL. No. 1993-4280.
20. Boardman, T. A., D. H. Brinton, R. L. Carpenter, and T. F. Zoladz. 1995. An experimental investigation of pressure oscillations and their suppression in subscale hybrid rocket motors. AIAA Paper No. 95-2689.
21. Boardman, T. A., R. L. Carpenter, and S. A. Claflin. 1997. A comparative study of the effects of liquid- versus gaseous-oxygen injection on combustion stability in 11-inch-diameter hybrid motors. AIAA Paper No. 1997-2936.
22. Shimada, T. 2012. Status summary of FY 2011 Hybrid Rocket Research Working Group. *9th Conference (International) on Flow Dynamics*. Sendai, Japan.
23. Bettella, A., F. Moretto, E. Geremia, N. Bellomo, D. Petronio, and D. Pavarin. 2013. Development of 20 kN hybrid rocket booster. *5th European Conference for Aeronautics and Space Sciences*. Munich, Germany.
24. Karabeyoglu, M. A., D. Altman, and B. J. Cantwell. 2002. Combustion of liquefying hybrid propellants: Part 1, general theory. *J. Propul. Power*. 18(3):610–620.
25. Kobald, M., C. Schmierer, H. Ciezki, S. Schlechtriem, E. Toson, and L. T. De Luca. 2014. Evaluation of paraffin-based fuels for hybrid rocket engines. AIAA Paper No. 2014-3646.
26. Fischer, U. 2014. Design of a CFRP-pressure vessel for a sounding rocket. Stuttgart University. Studienarbeit.

27. Karabeyoglu, M. A., J. Dyer, J. Stevens, and B. Cantwell. 2008. Modeling of N_2O decomposition events. AIAA Paper No. 2008-4933.
28. Tomilin, K. 2014. Design of an automatic recovery system for a sounding rocket. Stuttgart University. Studienarbeit.
29. Lobanov, N. A. 1965. *Osnovy rascheta i konstruirovaniya parashutov* [Basics of calculation and design of parachute system]. Moscow: Mashinostroenie. 356 p.
30. Kobald, M., C. Schmierer, and A. Petrarolo. 2015. Test campaign of a 10000 N hybrid rocket engine. *European Conference for Aeronautics and Space Sciences*. Krakow, Poland.
31. Karabeyoglu, M. A., B. J. Cantwell, and G. Zilliac. 2007. Development of scalable space–time averaged regression rate expressions for hybrid rockets. *J. Propul. Power* 23(4):737–747.
32. Sutton, G. P., and O. Biblarz. 2001. *Rocket propulsion elements*. John Wiley & Sons, Inc. 764 p.
33. Karabeyoglu, M. A., S. De Zilwa, B. Cantwell, and G. Zilliac. 2005. Modeling of hybrid rocket low frequency instabilities. *J. Propul. Power* 21(6):1107–1116.
34. Carmicino, C. 2009. Acoustics, vortex shedding, and low-frequency dynamics interaction in an unstable hybrid rocket. *J. Propul. Power* 25(6):1322–1335.
35. Kobald, M., E. Toson, H. Ciezki, S. Schlechtriem, S. Di Betta, M. Coppola, and L. T. De Luca. 2013. Rheological, optical and ballistic investigations of paraffin-based fuels for hybrid rocket propulsion using a 2D slab-burner. *5th European Conference for Aeronautics and Space Sciences*. Munich, Germany.
36. Toson, E., M. Kobald, S. Di Betta, L. T. De Luca, H. Ciezki, and S. Schlechtriem. 2013. Rheological and ballistic investigations of paraffin-based fuels for hybrid rocket propulsion using a 2D radial micro-burner. *5th European Conference for Aeronautics and Space Sciences*. Munich, Germany.
37. Zilliac, G., and M. A. Karabeyoglu. 2006. Hybrid rocket fuel regression rate data and modeling. AIAA Paper No. 2006-4504.
38. Doran, E., J. Dyer, K. Lohner, Z. Dunn, B. Cantwell, and G. Zilliac. 2007. Nitrous oxide hybrid rocket motor fuel regression rate characterization. AIAA Paper No. 2007-5352.
39. Grosse, M. 2009. Effect of a diaphragm on performance and fuel regression of a laboratory scale hybrid rocket motor using nitrous oxide and paraffin. AIAA Paper No. 2009-5113.